Target Three-Dimensional Reconstruction From the Multi-View Radar Image Sequence

YEJIAN ZHOU [1,2], **LEI ZHANG** [1,2,3], **CHAO XING** [1,2], **PENGFEI XIE** [1,2], **AND YUNHE CAO** [1,2]

[1] National Laboratory of Radar Signal Processing, Xidian University, Xi'an 710071, China
[2] Collaborative Innovation Center of Information Sensing and Understanding, Xidian University, Xi'an 710071, China
[3] School of Electronics and Communication Engineering, Sun Yat-sen University, Guangzhou 510275, China

Corresponding author: Lei Zhang (leizhang@xidian.edu.cn)

ABSTRACT Target three-dimensional (3D) reconstruction is a hot topic and also a challenge in remote sensing applications. In this paper, a new reconstruction algorithm is proposed to reconstruct the 3D surface of the stable attitude target from its multi-view radar image sequence. Uniform explicit expression of the radar and optical imaging geometries is derived to bridge the 3D target structure and these two sorts of observation images. In this way, the visual hull of the target is reconstructed by exploiting the multi-view stereo techniques to the silhouette information extracted from the radar image sequence. Meanwhile, the target absolute attitude is also determined. Furthermore, we analyze the primary difficulty of the method induced from the limited radar observation view in a typical application, the 3D reconstruction of an in-orbit satellite. Then, an extended algorithm is proposed with the feature fusion of the radar and optical images to achieve dramatic performance enhancement of the reconstruction in this condition. The feasibility of the proposed algorithm is confirmed in the experiment part, and some conclusions are drawn to guide the future work about extended applications of the proposed algorithm as well.

INDEX TERMS Radar imaging, geometrical projection, three-dimensional reconstruction, feature fusion of the radar and optical images.

I. INTRODUCTION

With the development of high-resolution imaging techniques, three-dimensional (3D) reconstruction of the observed target plays a more and more important role in various remote sensing applications, such as satellite health monitoring, geological surveying and target recognition [1]–[15]. Thanks to the robust working capability in the all-day and all-weather circumstances, radar is employed to accomplish these tasks through interpreting high-resolution radar images.

The predominant work of this paper focuses on the effective rebuilding of the 3D satellite structure for space applications. In order to accomplish the task, inverse synthetic aperture radar (ISAR) technique is usually adopted [1]–[11]. In [7], measured ISAR images acquired by the Tracking and Imaging Radar (TIRA) were matched with the full-view simulation images to determine the attitude information of the in-orbit Envisat satellite. In [8], extracted from multi-

view ISAR images, the scattering point feature of a shuttle was used to retrieve its 3D structure by the classical factorization algorithm. However, some technological complexities and difficulties, like the scattering points association among the multi-view images, limit the performances of these algorithms. Besides, as an essential factor of radar imaging, the diversity of synthetic aperture manifold has a direct impact on the performance of the 3D information analysis. In some particular observations, such as the long-time observation of an in-orbit satellite based on ground radars, it is hard to analyze target 3D information when the angular source of radar observation is limited [9]. In current literatures, there are some successful works on 3D imaging radar [12]–[15]. For example, an X-band wideband radar is used to generate 3D images of vehicles by radar cross-section imaging [12]. And for measuring the growth of volcanic lava domes, the lava dome surface is reconstructed by real aperture radars, which usually loaded on a jeep or helicopter, in a 3D scanning way [13]. To some degree, the image interpretation manners in these works are close to the processing technique

---

The associate editor coordinating the review of this manuscript and approving it for publication was Wen Chen.

of optical data, which provides a fresh perspective of rebuilding satellite 3D structure from ISAR images.

In this paper, we propose a 3D reconstruction algorithm to rebuild the 3D surface of a stable attitude satellite based on the multi-view radar image sequence. First, a geometric model of the radar imaging is developed combined with the imaging projection theory [17]. Then, compared with the affine model of the optical imaging senor, an explicit expression is derived to bridge the 3D structure of the target with two-dimensional (2D) radar imagery. With the accommodation of multi-view stereo techniques in computer-vision (CV) field [18]–[25], the 3D visual hull is built to represent the target surface with the silhouette information extracted among the multi-view image sequence. Besides, in order to enhance the reconstruction performance in the limited radar observation view (as mentioned above), the proposed algorithm is further expanded with a feature fusion strategy of the radar and optical images. The fusion of optical and radar images, is widely employed in various practical applications [26]–[33]. For instance, the chemical composition and structural elements of the land cover, provided by the optical sensor and synthetic aperture radar (SAR) respectively, were fused to estimate sagebrush, herbaceous, and bare ground cover in Yellowstone [31], [32]. In this work, this fusion strategy is based on the perpendicularity between these two sorts of imaging planes in the same observation view to analyze 3D information of the target.

Compared with the existing methods, the proposed algorithm has some innovations as follows.

1) From the 3D reconstruction result, most relevant literature adopts factorization algorithm to retrieve target 3D structure without the size constraint, resulting in the scaling difficulty of their reconstruction results [4]–[6], [8]. By contrast, the proposed algorithm draws a 3D visual hull and meanwhile determines its size and attitude information as the radar line of sight (LOS) parameters and image resolutions are taken into consideration. Particularly, target attitude which can not be solved by other methods plays an essential role in some practical applications.

2) To our knowledge, it is the first time that the radar and optical images have been fused for the sake of target 3D reconstruction. As the radar and optical image sequences are simultaneously generated in a same observation view, the geometrical imaging planes are perpendicular, providing complementary geometrical information of the target in each moment. It paves the way to acquire extra 3D information of targets when the angular source of radar is limited. The extension shows explicit advantages of the multi-sensor information fusion in space applications.

3) Compared with the scattering point feature, the silhouette feature used in this work is readily extracted and associated among the multi-view radar image sequence when the angular glint phenomenon occurs [16]. The proposed algorithm also can be performed with the mix feature of target silhouette and key points (like the corners), which enhances the structure characteristics of the reconstruction result in some specific tasks.

4) Although the proposed algorithm predominantly serves as the 3D reconstruction of satellite target in the current stage, it can be expanded to various practical applications. In the last experiment, a human body is reconstructed with the measurement circular synthetic aperture radar (CSAR) imagery in a security inspection occasion. From the aspect of relative motion between the radar and target, the proposed algorithm can be directly applied to interpret both SAR and ISAR imagery when the synthetic aperture manifold is determined in advance. However, some extra processing details need to be handled due to the different application characteristics, like the image registering, which are analyzed in the Conclusion.

The remainder of this paper is organized as follows. Section II compares the imaging geometries of optical sensor and radar, and an explicit expression is derived to unify the imaging representation of these two sorts of sensors. Section III presents the details of the proposed 3D reconstruction method. Four experiments are provided in Section IV to illustrate the feasibility and advantages of the proposed algorithm. Finally, Section V gives some conclusions and plans our future work.

II. IMAGING GEOMETRIES OF OPTICAL AND RADAR SENSORS

In this section, the connection between the target 3D structure and its radar imagery is analyzed according to the LOS parameters. Combined with the imaging geometry of optical camera, a uniform math expression of imaging processing is concluded for these two sensors. It paves a way to reconstruct target 3D structure and meanwhile determine its attitude from a multi-view radar image sequence, and is also beneficial to make a feature fusion of these two sorts of images in subsequent sections. The detailed derivations are below.

A. THE PROJECTION MODEL OF RADAR IMAGING

The radar echo signal of a solid target can be expressed by the superposition of isolated point scattering responses. When the conventional range compression and range cell migration correction are well performed, it can be written as [34]

$$S(t_s, t_m) = \sum_{p=1}^{N} \text{sinc}(t_s - \tau_p) \times \text{rect}\left[\frac{t_m}{T_m}\right]$$
$$\times \exp\left[-\frac{j4\pi R_p(t_m)}{\lambda}\right] \quad (1)$$

where $\text{sinc}[u] = \sin(\pi u)/(\pi u)$ refers to the Sinc function, $\text{rect}[\bullet]$ represents the rectangle window function, t_s denotes the fast-time relative to the sampling in the range direction while t_m denotes the slow-time relative to the sampling in the azimuth direction, p is the serial number of scattering points, τ_p is the time-delay of a scattering point in current pulse,
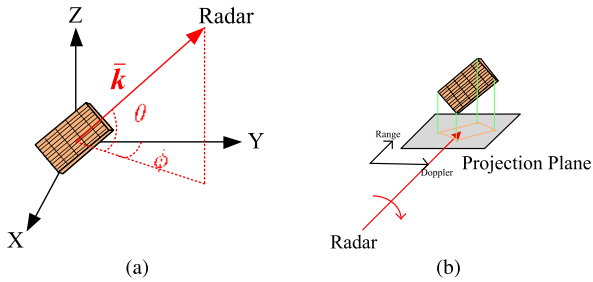
FIGURE 1. The ISAR imaging geometry: (a) The radar observation geometry in the target Cartesian coordinates; (b) The projection plane of a single image during the current CPI.

FIGURE 2. The affine plane of optical imaging processing.

T_m denotes the pulse duration width, λ represents the signal wavelength, and $R_p(t_m)$ refers to the instantaneous distance of the scattering center.

Because both SAR and ISAR images are based on the relative motion between the radar and target, we use the uniform model that the target is fixed while the radar moves to express the motion geometry of radar imaging in this paper. When the relative translation between target and radar is compensated well, the instantaneous distance of a certain scattering center is determined by the inner product between its 3D position and the instantaneous LOS unit vector in the target Cartesian coordinates [9], [10], [17]. As the scattering points position is assumed to be fixed, the relative rotation is represented by the equivalent rotation of the instantaneous LOS unit vector $\vec{k}(t_m)$ as

$$R(t_m) = \vec{p}\vec{k}(t_m) \approx \vec{p}\left[\vec{k}_0 + \vec{k}'t_m + \vec{k}''t_m^2\right]$$
$$= R_0 + R't_m + R''t_m^2 \qquad (2)$$

where the scattering center position is defined as $\vec{p} = (x, y, z)^T$, the instantaneous distance is composed of the initial term R, first order term R', and quadratic term R''.

In practical applications, the instantaneous LOS unit vector $\vec{k}(t_m)$ is determined by two LOS parameters, the elevation angle $\theta(t_m)$ and the azimuth angle $\phi(t_m)$ as shown in Fig. 1(a), which are generally recorded in the radar tracking system.

$$\vec{k}(t_m) = (\cos\theta(t_m)\sin\phi(t_m),$$
$$\cos\theta(t_m)\cos\phi(t_m), \sin\theta(t_m))^T \qquad (3)$$

As is known, radar, as an essential sensor for distance measurement, only records the one-dimensional distance history $R(t_m)$ while the other dimensional information depends
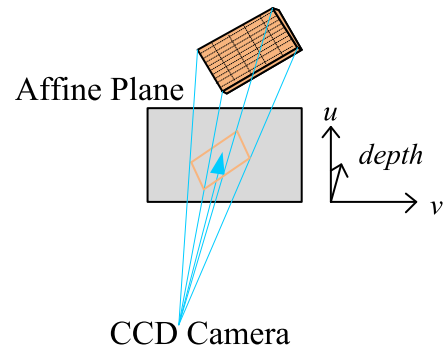
on analyzing the frequency characteristics of the echo signal in single coherent processing interval (CPI). Concretely, an azimuth compression is executed in the slow-time domain with an FFT processing. Combined with Eq. (2), the radar imagery is expressed as Eq. (4), as shown at the bottom of this page.

For this reason, the radar (both SAR and ISAR) image generated by the conventional Range-Doppler (RD) algorithm is also called RD image. And the generation of these two sorts of images only have some technical differences in processing, such as motion compensation.

Most relevant studies pay dominating attention to the improvement of the image quality while a further interpretation of the target structure and state can be realized by utilizing the radar imaging geometry. When the radar imaging is understood as the stable attitude target being projected in an imaging plane, as shown in Fig. 1(b), both the two directions of a RD image can be calculated with the LOS parameters. In the condition of stable imaging, the geometric manifold of synthetic aperture during a single CPI is not undulated. As a result, the imaging plane of radar imaging corresponds directly to a physical 2D plane in the true 3D world: the range direction of the image is determined by the center LOS unit vector while the azimuth direction refers to the differential coefficient of the LOS vector in the middle moment t_0 of the CPI. And the projection position of a scattering point in the RD image $(r, d)^T$ is expressed as Eqs. (5)-(6), as shown at the bottom of the next page.

It should be emphasized that the interpretation of radar imagery in this paper is based on the high quality imagery of the stable attitude target. From the published measured radar imagery [35], this premise is accredited in practical applications, and the imaging geometry calculation of radar synthetic

$$S(t_s, f_d) = \sum_{p=1}^{N} \text{sinc}(t_s - \tau_0) \times \text{FFT}\left[\text{rect}\left[\frac{t_m}{T_m}\right] \times \exp\left[-\frac{j4\pi R(t_m)}{\lambda}\right]\right]$$
$$= \sum_{p=1}^{N} \text{sinc}(t_s - \tau_0)\text{sinc}\left(f_d - \frac{2\pi R'}{\lambda}\right)A_1(f_d, R'') \qquad (4)$$

where $A_1(f_d, R'')$ is the unfocusing of the scattering point caused by the distance quadratic term R''.

B. THE AFFINE MODEL OF CAMERA IMAGING

It is known that, the imaging processing of the optical system, whether CCD camera or eyes, is based on a physical mechanism called affine, as depicted in Fig. 2. It is described as the reflected ray of the solid object passing through the affine plane and arriving at the center of the optical sensor; meanwhile, it leaves a 2D shrunken optical image in the affine plane. In the CV field, the scaling matrix is applied to represent the mapping between target coordinates in the optical imagery and its coordinates in the 3D world [36].

$$\begin{pmatrix} u \\ v \\ 1 \end{pmatrix} = A_{optical} \bullet \vec{p} \qquad (7)$$

where $(u, v)^T$ is the two-dimensional coordinates of a certain point in the optical imagery, and the scaling matrix $A_{optical}$ is related to three-part parameters, including the relative position between cameras, the focal lengths of two image directions and the resolution of the imagery [36]–[38].

During the multi-view observation scenarios, the essential matrix, which contains information about the relative position and orientation between two different cameras, is applied to analyze the affine geometrical connection in different observation views.

$$A'_{optical} = \hat{T} R A_{optical} \qquad (8)$$

where $\hat{T}$ is a linear transformation to represent the translation of the camera center, and R is an Euler rotation matrix to reflect the different observation views.

C. THE UNIFORM MATH EXPRESSION OF RADAR AND CAMERA IMAGING

Although these two types of imaging processing are different in the essence, the imaging geometry of each sensor can be determined by a projection matrix. It bridges the 3D information of the target and the obtained image sequence, and can be calculated accurately in practical applications. The acquirement of radar projection matrix A_{radar} is discussed above, and the calculation of optical projection matrix $A_{optical}$, also called the camera calibration, is introduced in relevant literature [36]–[38]. Thus, the uniform math expression of radar
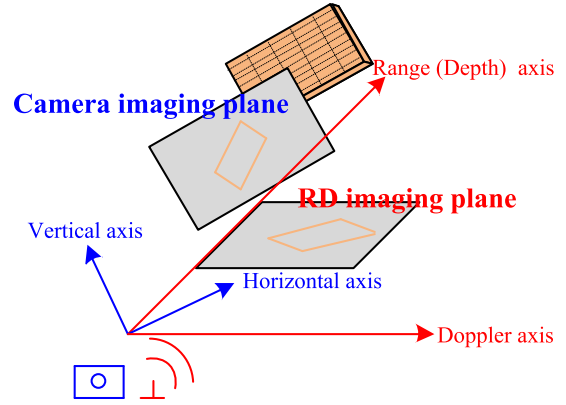

FIGURE 3. Comparison between two kinds of imaging geometry.

and camera imaging is given below

$$\vec{p}_{image} = A_{optical} \bullet \vec{p} \qquad (9)$$

When $\vec{p}_{image}$ refers to the coordinates $(r, d)^T$ in the radar imagery, the projection matrix A corresponds to the projection matrix A_{radar}. When $\vec{p}_{image}$ refers to the coordinates $(u, v)^T$ in the optical imagery, the projection matrix corresponds to the scaling matrix $A_{optical}$.

However, there is a conspicuous distinction that the projection planes of these two sorts of imaging method are perpendicular in the same observation view. As shown in Fig. 3, two image axes (vertical axis and horizontal axis) are perpendicular to the depth axis in the optical imaging geometry while the range axis is always in the RD imaging plane in the radar imaging processing. Therefore, the target projection information in radar and camera imaging planes are complementary, and the feature fusion of these two sorts of image sequence is beneficial to the 3D reconstruction of a stable attitude target when the angular scope of radar observation is not sufficient.

III. THREE-DIMENSIONAL RECONSTRUCTION FROM SILHOUETTE INFORMATION

A. THE FLOWCHART OF THE PROPOSED ALGORITHM

The proposed algorithm predominantly serves as the 3D reconstruction of a stable attitude target, like the in-orbit satellite, and its flowchart is illustrated in Fig. 4. First, a multi-view radar image sequence is generated and the projection

$$\begin{pmatrix} r \\ d \end{pmatrix} = A_{radar} \bullet \vec{p} = \begin{pmatrix} \dfrac{\vec{k}(t_0)}{\Delta r} \\ \dfrac{\vec{k}(t_0)}{\Delta f_d} \end{pmatrix} \bullet (x, y, z)^T \qquad (5)$$

$$\vec{k}'(t_0) = \begin{pmatrix} -\sin\theta(t_0)\sin\phi(t_0)\,\theta'(t_0) + \cos\theta(t_0)\cos\phi(t_0)\,\phi'(t_0) \\ -\sin\theta(t_0)\cos\phi(t_0)\,\theta'(t_0) - \cos\theta(t_0)\sin\phi(t_0)\,\phi'(t_0) \\ \cos\theta(t_0)\,\theta'(t_0) \end{pmatrix}^T \qquad (6)$$

where $\Delta r = c/2f_s$ denotes the range pixel resolution of RD images, c is the speed of light, $\Delta f_d = \lambda/2\Delta T$ denotes the Doppler bin resolution of RD images, ΔT refers to the CPI of the current image.
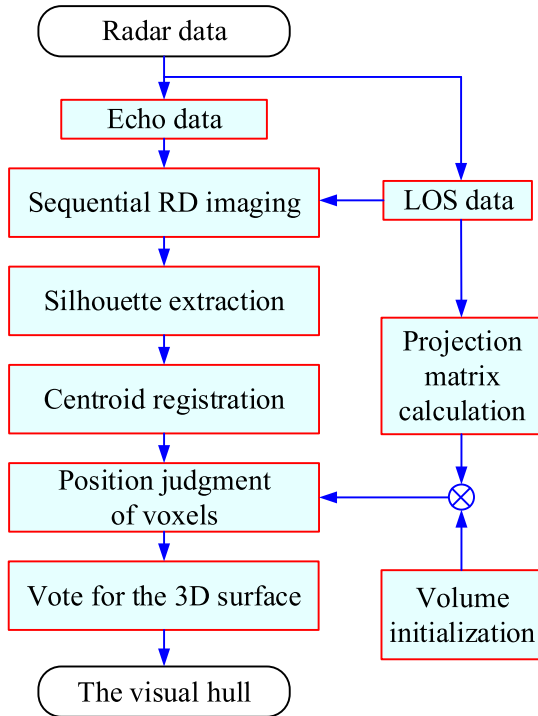
FIGURE 4. The flowchart of the proposed algorithm.

matrix sequence are also calculated according to the LOS parameters in the radar tracking system. Then, some image processing techniques are employed to extract the silhouette information in the radar image sequence. After the volume initialization, based on the imaging projection Eq. (9), each voxel in an initial volume is projected in the current imaging plane to judge whether it is a voxel inside of the observed target or not. Finally, with the judgment processing executed in each image, a visual hull is voted to represent the 3D surface of the reconstructed target. The details are given in following subsections.

B. THE OPTIMAL DIVISION OF RADAR ECHO DATA FOR THE RD IMAGE SEQUENCE GENERATION

First, a high-resolution image sequence of the target is generated with the sequential radar echo data by RD algorithm [34]. In order to ensure the precision of the reconstruction, it is suggested that the image resolution of the RD image sequence be approximate to a constant. The range resolution of a radar image relies on the range sampling while the azimuth resolution depends on the observation angle accumulated within the current CPI. According to the LOS parameters recorded in the tracking system, the azimuth resolution of a single RD image can be determined by

$$\Delta f_a = \lambda / 2 \Delta \delta \qquad (10)$$

where $\Delta \delta$ is the angular integral of the instantaneous LOS unit vector $\vec{k}(t_m)$ during the current CPI. In the azimuth direction, the numerical conversion between Δf_d and Δf_a is

$$\Delta f_d = \bar{w} \Delta f_a \qquad (11)$$

where $\bar{w}$ refers to the mean rotation rate of the LOS vector during the current CPI.

Beside the resolution demands, pursuing a well focusing performance of the high-resolution imagery is also an imperative factor in guiding the division of the received echo data. In the target Cartesian coordinates, the range difference on the target surface can be defined as Eq. (12), shown at the bottom of this page.

Generally, $\theta(t_m)$ and $\phi(t_m)$ can be approximated to quadratic curves in a single CPI.

$$\theta(t_m) = \theta_0 + \theta' t_m + \frac{1}{2} \theta'' t_m{}^2 = \tilde{\theta} + \Delta \theta (\theta'') \qquad (13)$$

$$\phi(t_m) = \phi_0 + \phi' t_m + \frac{1}{2} \phi'' t_m{}^2 = \tilde{\phi} + \Delta \phi (\phi'') \qquad (14)$$

where $\tilde{\theta}$ is the expected $\theta(t_m)$, $\tilde{\phi}$ is the expected $\phi(t_m)$, $\Delta \theta(\theta'')$ is the error caused by θ'', $\Delta \phi(\phi'')$ is the error caused by ϕ'', and $-\frac{\Delta T}{2} \leq t_m \leq \frac{\Delta T}{2}$.

Combining Eqs. (12)-(14), the maximum range difference caused by the second derivative of $\theta(t_m)$ and $\phi(t_m)$ (i.e. θ'' and ϕ'') can be calculated.

$$\Delta(\theta'', \phi'') = R(\tilde{\theta} + \Delta \theta(\theta''), \tilde{\phi} + \Delta \phi(\phi'')) - R(\tilde{\theta}, \tilde{\phi}) \qquad (15)$$

In practical applications, the maximum phase difference $\Delta \varphi(\theta'', \phi'')$ in a target surface should meet the following condition.

$$\Delta \varphi(\theta'', \phi'') = \left| \frac{4\pi}{\lambda} \Delta R(\theta'', \phi'') \right| \leq \frac{\pi}{4} \qquad (16)$$

All in all, the division principle is that the second derivatives of $\theta(t_m)$ and $\phi(t_m)$ ought to be approximate to constants during the current CPI for the imaging requirement. In practice, this requirement can hardly be met, and an acceptable compromise is that the second derivatives of $\theta(t_m)$ and $\phi(t_m)$ should be within definite thresholds. And another empirical conclusion is summarized as the data segment in the zenith-passing duration is not suitable for the stable RD imaging of an in-orbit satellite where the second derivatives of $\theta(t_m)$ and $\phi(t_m)$ change rapidly. Therefore, the proposed algorithm needs to be performed avoiding this sort of data segment.

C. SILHOUETTE EXTRACTION FROM THE ISAR IMAGE SEQUENCE

Silhouette-based methods are widely employed in multi-view observation conditions due to their simplicity and robustness

---

$$R(\theta(t_m), \phi(t_m)) = b_x \cos\theta(t_m) \sin\phi(t_m) + b_y \cos\theta(t_m) \cos\phi(t_m) + b_z \sin\theta(t_m) \qquad (12)$$

where b_x, b_y and b_z represent coordinates of target size in the target Cartesian coordinate system. _____

of feature extraction and association [19]–[22]. Particularly in the radar observation of artificial targets, the scattering anisotropy caused by target material and structure makes local feature, like strong scattering points, dramatically changed in different views. By contrast, target silhouette feature is more robust in the 3D reconstruction tasks based on the multi-view radar images.

In view of the radar echo characteristics, the noise of a RD image, i.e. the background part, is normally distributed.

$$F(x) = \int_{-\infty}^{x} \frac{1}{\sqrt{2\pi}\sigma} \exp\left(\frac{(t-\mu)^2}{2\sigma^2}\right) dt \qquad (17)$$

where μ and σ are the mean and variance of the noise respectively. In practical processing, these two parameters can be directly used to classify the target and background pixels in the RD imagery. A typical approach to estimating these two parameters is the collaborative forecast and replenishment (CFAR) algorithm, which is widely adopted in the background segmentation of SAR and ISAR images [39]. In this paper, we simplify the conventional CFAR algorithm as follows.

- Step 1: Calculate the mean and variance of whole imagery.
- Step 2: Sort all the pixels into target and background classes according to the following threshold.

$$\text{Threshold} = \mu + a_1\sigma \qquad (18)$$

- Step 3: According to the classification result, the mean and variance of background pixels are calculated.
- Step 4: Sort the current background pixels into new background classes according to the new threshold.

$$\text{Threshold}' = \mu' + a_2\sigma' \qquad (19)$$

- Step 5: Calculate the new mean and variance of background pixels. If the mean change is less than a given termination value, break the iteration; otherwise, return to Step 4.

Empirically, the actors a_1 and a_2 are set to be 3 and 5, respectively.

As the segmentation result can be regarded as binary imagery, some classical boundary extraction techniques are readily applied to extract target silhouette, like morphological algorithms [40]. A method focusing on the local characteristic of the image (8-connected region) is used to describe the target feature in this work. However, different from optical imagery, the image quality is limited to its imaging processing and observation condition, resulting in the loss of pixel continuity (or called photo-consistency) in radar imagery [21]. It is still a challenge to automatically extract target silhouette in practical measurement. When target boundaries are fuzzy or discontinuous among measured radar images, it is acceptable to manually extract the silhouette information to ensure the reconstruction performance of the proposed algorithm.
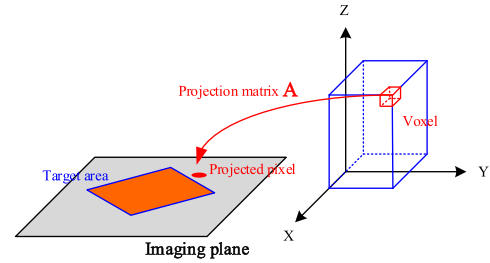

FIGURE 5. The projection relationship between the 3D target voxel and its 2D image.

D. VOTE OF 3D VISUAL HULL

As the observation geometry of continuous radar imaging can be determined with a series of projection matrix mentioned above, it becomes a classic vision problem to reconstruct the target 3D structure from multi-view images. Transforming the idea of multi-view stereo algorithms for the optical image sequence [18]–[20], we utilize the silhouette information of the radar image sequence to reconstruct a visual hull which reflects the target 3D characteristics.

First, centroid registration of the silhouette is executed among the image sequence. According to the LOS parameters in the tracking system, it can be guaranteed as the target is located near the image center after RD imaging processing.

Then, in the i-th RD image, the silhouette set G_i is composed of a series of edge points $\vec{b}'_j(r, d)$, which are arranged clockwise, to segment the target area from the image. As shown in Fig. 5, a certain voxel $\vec{p}(x, y, z)$ in the true 3D space can projected into the current RD imaging plane as

$$\vec{p}_{image}(r, d) = A_{radar} \bullet \vec{p}(x, y, z) \qquad (20)$$

The problem whether this 3D voxel is the part of the target or not has been translated to a graphics problem whether its projection coordinate is inside the silhouette set G_i in each RD image or not. It is a classical problem in CV field and is solved through the Matlab Image Processing Toolbox in this paper. This solving processing will be defined as the symbol '⊙' in the later content, and the details are below.

- Step 1: Calculate two-dimensional range of the silhouette set G_i and judge whether the point $\vec{p}_{image}(r, d)$ is out of the range. If it does, this point does not locate inside the target area, and output 0. Otherwise, turn to Step 2.
- Step 2: Calculate the each pointing vector $\vec{b}_j = \vec{b}'_j(r, d) - \vec{p}_{image}(r, d), j = 1, ..., J$, and $\vec{b}_{J+1} = \vec{b}_1$.
- Step 3: According to the pointing vector, the quadrant number of each edge point $Qu(j)$ is determined and recorded from 0 to 3.
- Step 4: Determine the sign of cross productions between the pointing vector $\vec{b}_j(r, d)$ and $\vec{b}_{j+1}(r, d)$.

$$\begin{aligned} \text{Sc}(j) &= \text{sign}(\vec{b}_j \times \vec{b}_{j+1}) \\ &= \begin{cases} 1 & if\ r_j d_{j+1} - r_{j+1} d_j > \varepsilon_i \\ 0 & if\ |r_j d_{j+1} - r_{j+1} d_j| \le \varepsilon_i \\ -1 & if\ r_j d_{j+1} - r_{j+1} d_j < -\varepsilon_i \end{cases} \end{aligned} \qquad (21)$$

where factor $\varepsilon_i = \max \{|r_1|, ..., |r_J|, |d_1|, ..., |d_J|\}$ $\times 6.6613 \times 10^{-16}$.

- Step 5: Calculate the quadrant difference of each edge point $DQu(j) = Qu(j) - Qu(j+1)$, and update it according to the rule below.

$$DQu(j) = \begin{cases} -1 & if\, Qu(j) = 3 \\ 2 \times Sc(j) & if\, |Qu(j)| = 2 \\ 1 & if\, |Qu(j)| = -3 \end{cases} \quad (22)$$

- Step 6: Calculate the summary of the quadrant difference sequence. If the summary does not equal to zero, the point is an inside point and output 1. Otherwise, it is not an inside point, and turn to Step 7.
- Step 7: Determine the sign of inner production between the pointing vector $\vec{b}_j(r,d)$ and $\vec{b}_{j+1}(r,d)$.

$$Inn(j) = sign(\vec{b}_j \bullet \vec{b}_{j+1})$$
$$= \begin{cases} 1 & if\, r_j d_{j+1} + r_{j+1} d_j > \varepsilon_i \\ 0 & if\, |r_j d_{j+1} + r_{j+1} d_j| \leq \varepsilon_i \\ 1 & if\, r_j d_{j+1} + r_{j+1} d_j < -\varepsilon_i \end{cases} \quad (23)$$

- Step 8: If there is any j when $Sc(j) = 0$ meanwhile $Inn(j) \leq 0$, this point is on the contour and also defined as the inside point in this paper. Therefore, the output is also 1. Otherwise, output 0.

After repeating this processing in the image sequence, the confidence function of the silhouette consistency constraint [21] can be expressed as follows.

$$J(x,y,z) = \sum_i \left(A_{radar} \bullet \vec{p}(x,y,z) \right) \odot G_i(r,d) \quad (24)$$

where $\odot$ expresses the judgment operation of whether the point belongs to the target area, the frame number in the multi-view image sequence $i = 1, ..., I$. It should be noted that this processing merely focuses on the binary silhouette information in this paper, whereas some pixel characteristics, like the pixel consistency, are not taken into consideration. We need to analyze the target structure and transmitted signal characteristics further before taking full advantage of pixel information among the multi-view radar image sequence.

According to the principle that all target voxels should be projected into the target area in each image, target voxels are determined with the following vote strategy.

$$C(x,y,z) = \{J(x,y,z) = Threshold\} \quad (25)$$

where the threshold is set to be I.

At last, the 3D visual hull of the reconstructed target voxels is extracted (which is performed by the function *isosurface.m* in the Matlab Image Processing Toolbox), and generally used to reflects the most visualized characteristic of the observed target and also provides target size. The 3D structural information can be directly employed in various remote sensing applications. The reconstructed visual hull also determines target absolute attitude in the target Cartesian coordinates, which is capable of analyzing target potential state in
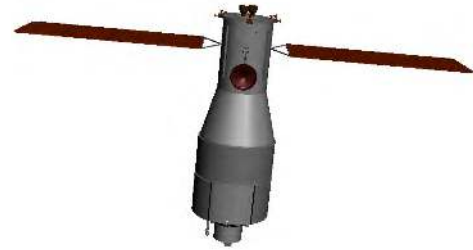

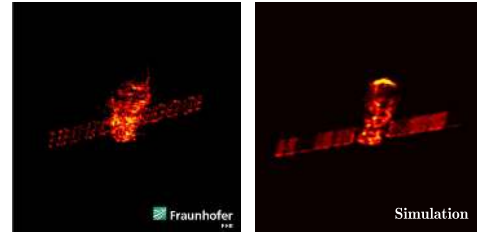**FIGURE 6.** The 3D model of the satellite target.

**FIGURE 7.** Visual comparison between the simulated and measured imagery.

space observations. Besides, the reconstruction method will be integrated with two sorts of mixed features, the optical-and-radar feature and the silhouette-and-component feature for different practical demands in the following experiments.

IV. EXPERIMENT ANALYSIS

In order to highlight the contributions of this paper, four experiments are performed to illustrate the feasibility and practical value of the proposed algorithm in two different application scenes. The experiment environment and contents are listed below.

- Part A: To prove its feasibility in ideal observation conditions, we reconstruct the 3D surface of a typical satellite with a large-angular-scope simulation image sequence in the first part.
- Part B: Then, we analyze how the limited observation angular scope affects the reconstruction performance of the proposed algorithm in a ground-based ISAR system, and propose an expansive algorithm by the feature fusion with synchronized optical images to ensure the reconstruction performance.
- Part C: In order to illustrate the superiority of the proposed algorithm, the analytical comparison experiment is performed with the factorization algorithm [8]. This experiment focuses on the comparison of target attitude and geometrical parameters extracted from the reconstructed 3D model. In this part, another complex satellite model is used, which confirms the feasibility of the proposed algorithm for most satellite targets.
- Part D: In the last part, we utilize the proposed algorithm to reconstruct the 3D visual hull of a human body with a measured CSAR image sequence, and the local component feature and silhouette information are taken into consideration for the security inspection.

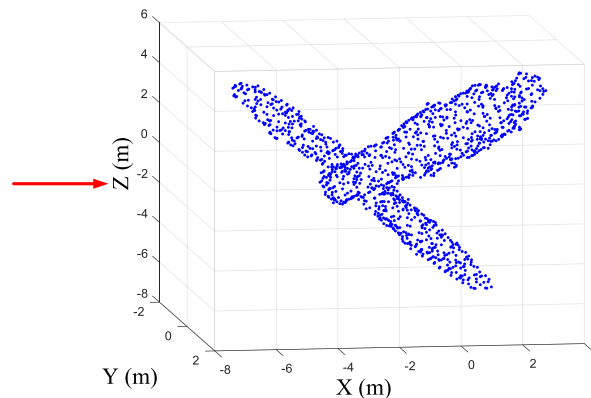Silhouette information
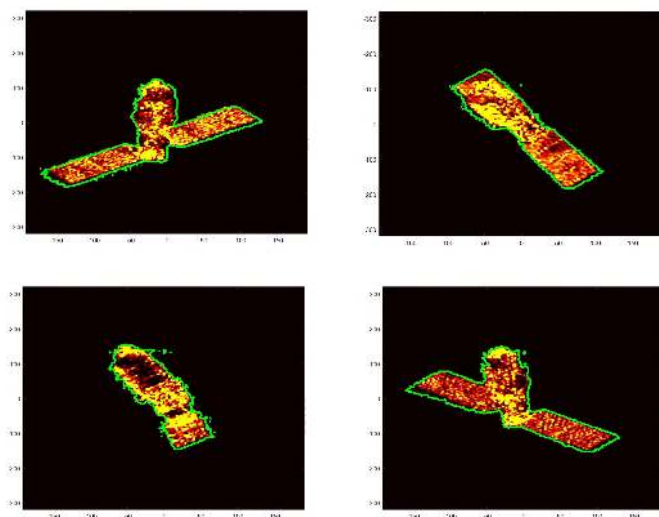
Reconstruction result

FIGURE 8. The 3D reconstruction result of the TG-I.

- Image sequences acquisition: The simulated image sequences are conducted in a Windows 7 Professional environment utilizing 2-core processors with Intel(R) Xeon (R) CPU E5-2603 v3,1.60 GHz,128GB RAM and the codes are implemented in Matlab R2015b. The ISAR imagery is generated by the improved physical optical algorithm [41], [42] while the simulation of the optical imagery is realized by the ray-tracing algorithm [43], [44]. The measured ISAR image sequence is obtained by a Ka-band radar system.

A. THE RECONSTRUCTION OF A SATELLITE IN THE LARGE OBSERVATION ANGULAR SCOPE CONDITION

In current stage, the proposed algorithm predominantly serves as reconstruction for an in-orbit satellite target based on the ground-based ISAR imagery. For lack of access to real measured ISAR data, the proposed algorithm is investigated with ISAR simulation images. In the experiment, a typical target Tiangong-I (TG-I), as shown in Fig. 6, is applied to generate simulation image by the improved physical optical algorithm. The main parameters of the ISAR system are listed in Table I. In Fig. 7, a visual comparison is provided between the simulation result and a measurement image published by German FGAN Lab in March, 2018 (@ Fraunhofer FHR) to prove the reliability of the simulated RD imagery [35]. In this experiment, a large observation angular scope condition is assumed, which means most area of the target surface appears among the ISAR image sequence. With the silhouette information by performing some image processing techniques [40], the reconstruction result of the target visual hull is obtained by the proposed method, as marked in green in Fig. 8. Compared with the 3D model given in Fig. 6, the reconstructed visual hull in Fig. 8 reflects the
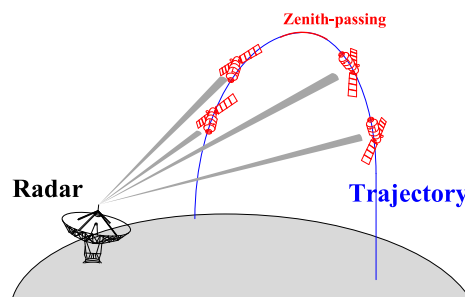
TABLE 1. The Main Parameters of the ISAR System.

Parameters	Value
Size of a single image	512×512
Wave length of transmit signal	0.018 m
Bandwidth	1 GHz
Center frequency of transmit signal	16.7 GHz
Pulse repetition frequency	100 Hz

FIGURE 9. The geometric model of continuous multi-view ISAR imaging.

most apparent characteristics of the observed target, which confirms the feasibility of the proposed algorithm.

B. THE RECONSTRUCTION OF A SATELLITE IN THE LIMITED OBSERVATION ANGULAR SCOPE CONDITION

The previous experiment confirms the feasibility of the proposed algorithm in the large observation angular scope condition. However, this condition might not be satisfied in most practical applications. In the previous study [10], it is found that only a limited area of satellite surface can be observed by a ground-based ISAR system, as shown in Fig. 9. As a result, the performance of the proposed algorithm can hardly
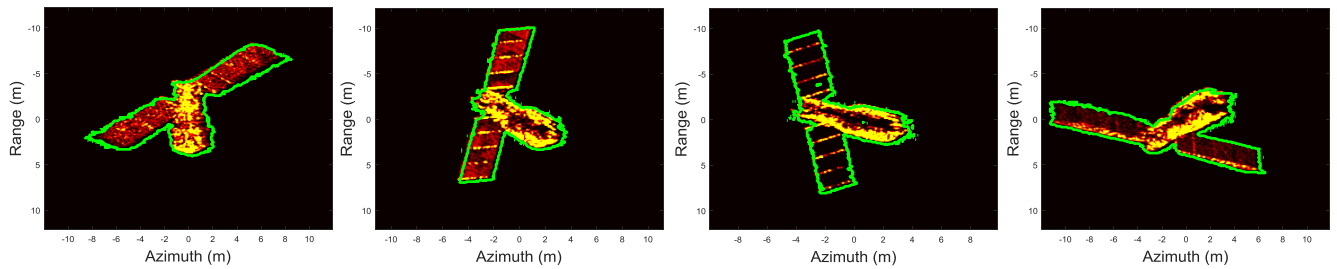
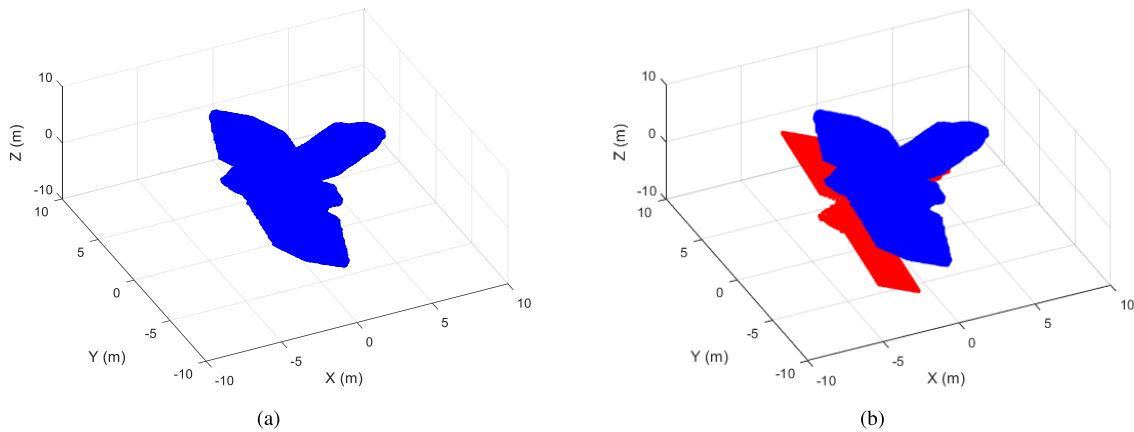**FIGURE 10.** The simulated ISAR image sequence of the TG-I.

FIGURE 11. The visual comparison of the 3D reconstruction result : (a) The reconstructed visual hull; (b) The visual comparison with the 3D model.

meet the demand of analyzing structure characteristic of the target. In this part, we adopt the measured tracking data of a 400-km height satellite to generate a simulated image sequence. The station is set at Beijing (39.9 N, 116.4 E, 88 m), and the azimuth and elevation angular scopes are 158.26 and 49.58 degrees, respectively. Four frames in the observation image sequence are given in Fig. 10, and the silhouette is extracted in each frame (marked green). The reconstruction result is given in Fig. 11(a). Compared with the true model marked red in Fig. 11(b), only some characteristics of the target surface is recovered due to the limited observation angular scope. This phenomenon is very common in the observation of in-orbit satellites but can be overcome through the feature fusion with the optical observation imagery.

As mentioned in Section II. C, the inherent perpendicular relation between radar and camera imaging planes makes it possible to obtain extra information at a single observation station. We use the ray-tracking algorithm to generate a synchronized optical image sequence at the same station [43], [44]. In this experiment, the horizontal direction of the optical image, which is always perpendicular to the range direction of the radar image, is assumed to coincide with the Doppler direction of the radar image at each moment. It is one possibility of the perpendicular relation between radar and camera imaging planes, but not a premise of the proposed fusion strategy.

From the optical image sequence in Fig. 12, although the same surface is irradiated by the electromagnetic wave

and visible light, the different recording methods result in different poses of the target projected in the imagery. Similar to the processing in the radar image sequence, the silhouette information is also extracted (marked red) and the affine matrix is calculated at each moment, as shown in the flowchart Fig. 13. Herein, perpendicular silhouette feature of these two sequences can be simultaneously obtained and jointly employed in the satellite 3D reconstruction at the single observation station. Through this feature fusion strategy, the confidence function Eq. (24) is expanded as Eq. (26), shown at the bottom of the next page.

As shown in Fig. 13(a), the shape and size features of the visual hull are close to the true values after the feature fusion of the radar and optical image sequences, and the absolute attitude of the reconstructed result also coincides with the true model (marked red) in Fig. 14(b). Compared with the reconstruction results in Fig. 11(b), it is proved that the feature fusion of the optical and radar imagery provides sufficient silhouette information to ensure the reconstruction performance without adding additional observation stations, which also highlights the advantage of the multi-sensor information fusion in space applications.

C. THE COMPARISON EXPERIMENT WITH THE FACTORIZATION ALGORITHM

In order to illustrate the superiority of the proposed algorithm in attitude and geometry analysis of satellite targets, the factorization algorithm [8] is performed to rebuild the 3D
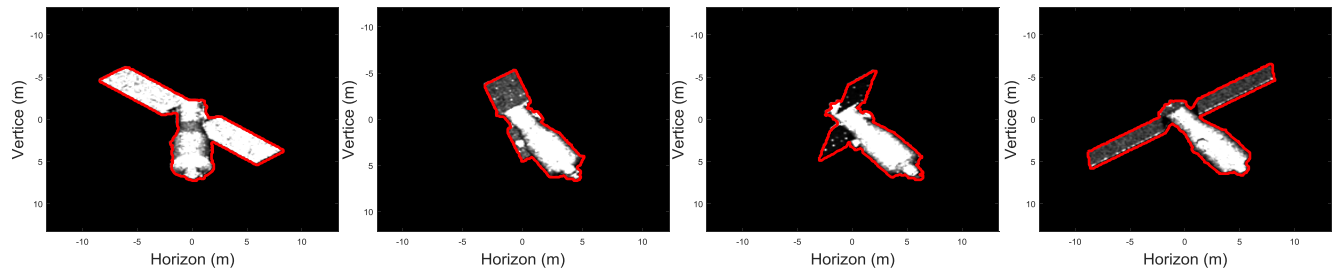
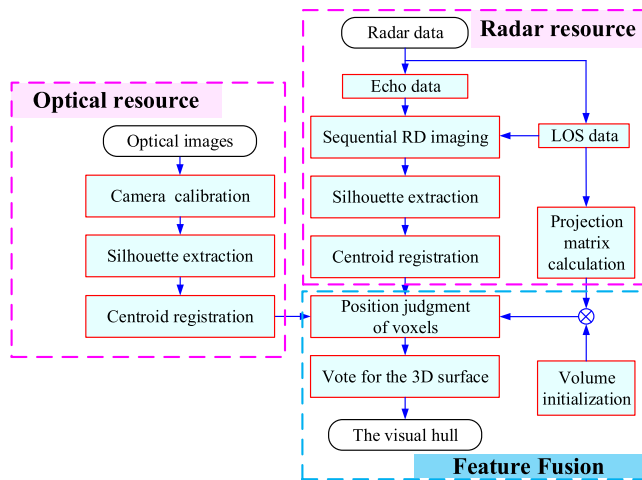**FIGURE 12.** The simulated optical image sequence of the TG-I.

FIGURE 13. The flowchart of the feature fusion of the optical and radar images.

distribution of 755 scattering points in the same observation condition of previous experiment. As shown in Fig. 15(a), Mars Reconnaissance Orbiter (MRO) is adopted as the target in this part experiment which also confirms the feasibility of the proposed algorithm for most satellite targets. It should be noted that the 3D reconstruction of the factorization algorithm is based on the correct association of each scattering point feature among the observation image sequence. In practical application, It is the crux of the performance of this sort of reconstruction method as the angular glint phenomenon [16] is common in an ISAR image sequence.

The reconstruction results of these two kinds of methods are shown in Fig. 15(c) and (d), respectively. Compared with the true 3D model of MRO shown in Fig. 15(b), the biggest difference between these two reconstruction results is whether the coordinates of the target construction are determined or not. Due to the limited connection between the factorization algorithm and the observation geometry [8]–[10], the target attitude and sizes can not be retrieved

in this way. It is the reason of the lack of axes definition in Fig. 15(c). By contrast, these 3D information can be determined by the proposed algorithm as shown in Fig. 15(d).

Besides the visual comparison in Fig. 15, the numerical comparison of the reconstruction results are also listed in Table II. In fact, both the visual 3D surface and point-cloud are just intermediate results. Based on these 3D model, the length or attitude parameters of key components need to be determined to analyze the target 3D information. In this part experiment, beside the length and attitude parameters of line features l_1, l_2 and l_3, the scale factors b_1 and b_2 are also defined by the ratio between lengths of two line features to describe target construction information. As listed in the Table. II, the mean length error of the proposed algorithm is 2% ($\left(\frac{|28.63-27.69|}{27.69} + \frac{|57.89-58.12|}{58.12} + \frac{|16.26-15.88|}{15.88} \right) \Big/ 3$) and its attitude estimation results also coincide with the true values. Both the calculated scale factors of the factorization and proposed algorithm are close to the true model. However, from the aspect of analyzing the target information, the proposed algorithm has more merits.

D. THE RECONSTRUCTION OF A HUMAN BODY WITH THE MEASUREMENT IMAGERY

Another essential application is to reconstruct some solid objects, like the human body, in some security inspection cases. In this experiment, a Ka-band measured CSAR image sequence is applied to reconstruct the visual hull of a human body in order to reflect its application values. The main parameters of the SAR images are listed in Table III. Under a circular scanning observation, the azimuth angular domain is 120 degrees and the elevation angle is fixed covering the front surface of the body according to the recorded LOS data. It means the obtained image sequence covers sufficient angular scope to recover most apparent characteristics of the human body, such as the height and the shoulder width. Although the protective cover leads to the low quality imaging performance as shown in Fig. 16, a comparatively

$$J(x, y, z) = \frac{1}{2} \sum_i \left(A_{i,radar} \bullet p(x, y, z) \right) \odot G_i(r, d) + \left(A_{i,optical} \bullet p(x, y, z) \right) \odot G_i'(u, v) \qquad (26)$$

where $G_i'(u, v)$ is the silhouette set extracted from the i-th optical image.
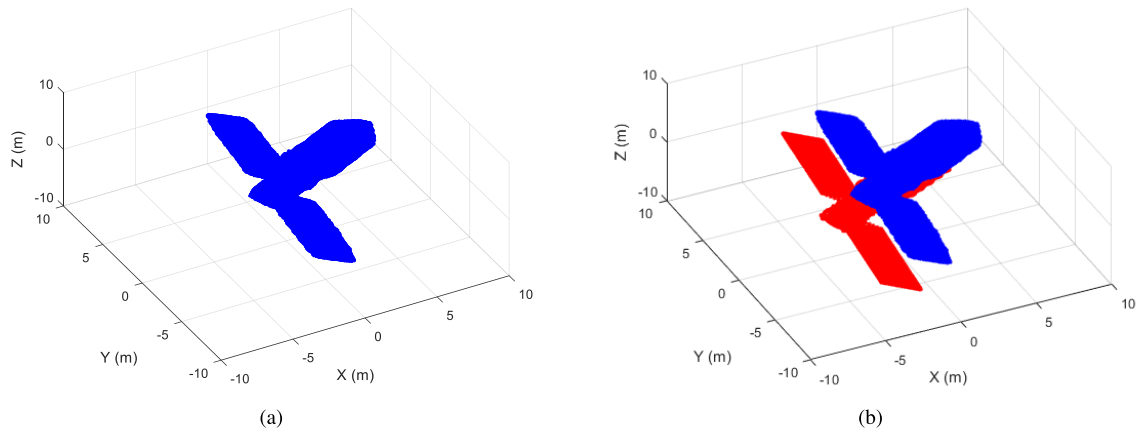
FIGURE 14. The visual comparison of the 3D reconstruction result : (a) The reconstructed visual hull; (b) The visual comparison with the 3D model.
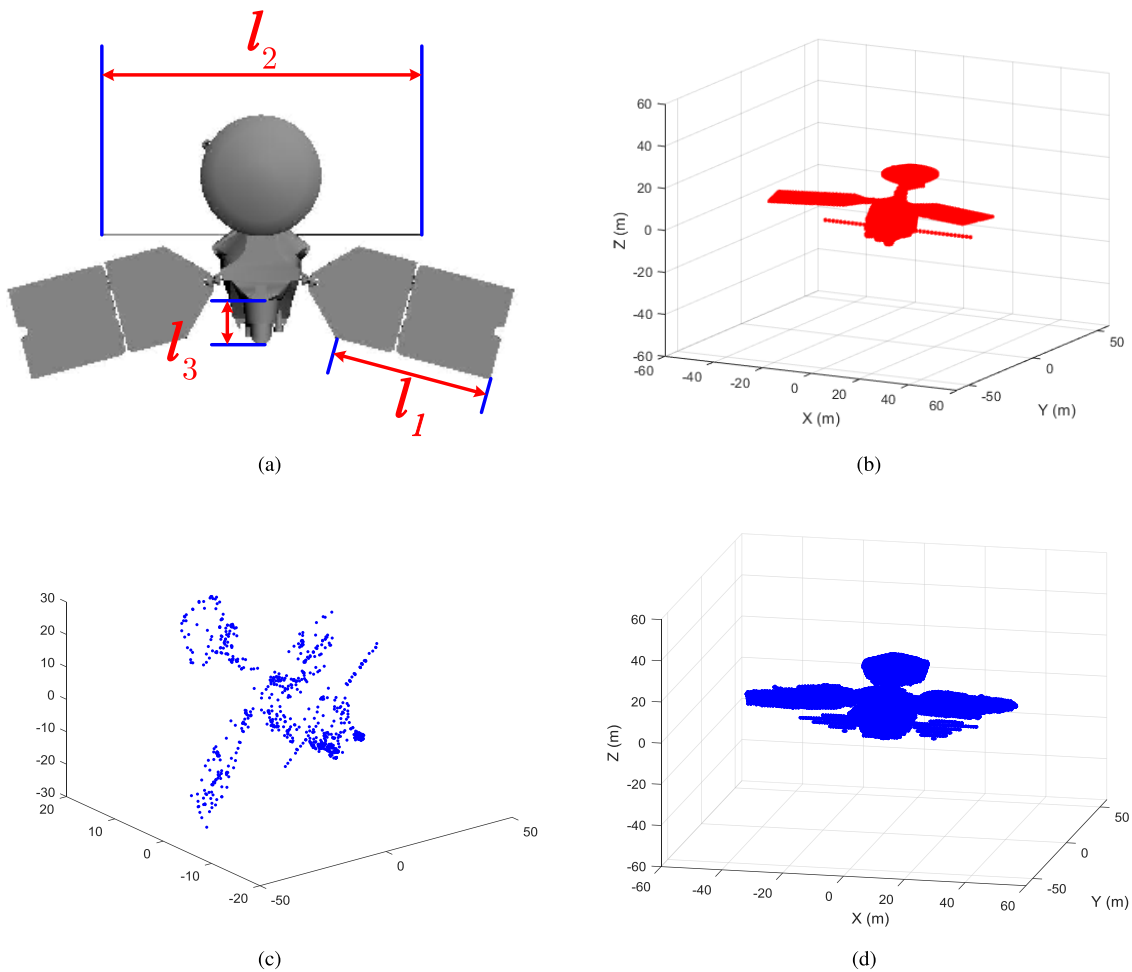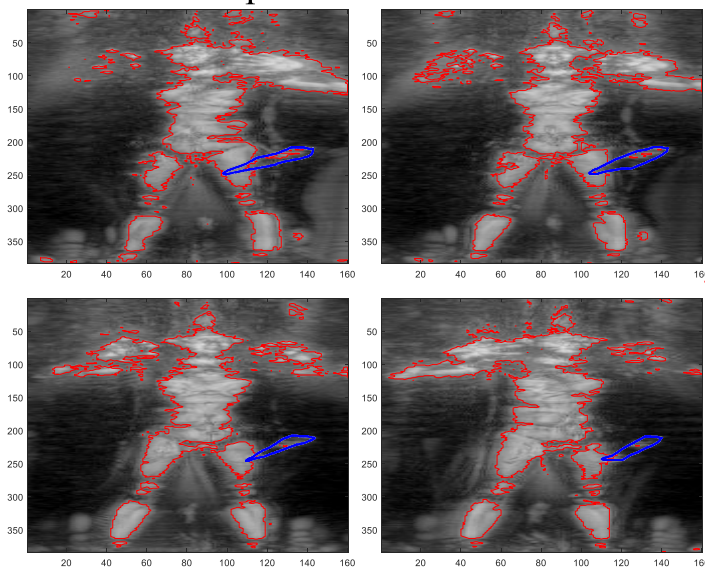

FIGURE 15. Comparison of reconstruction results: (a) The 3D model of MRO; (b) The true attitude model of MRO; (c) The reconstruction result of the factorization algorithm; (d) The reconstruction result of the proposed algorithm.

complete visual hull of the human body is reconstructed (marked red) from the extracted silhouette information yet. Measured from the reconstructed visual hull, the height and shoulder width are 1.73 m and 0.43 m, respectively, which are close to the true values. Besides the human body, a knife is also manually extracted among the image sequence (marked blue) as the local feature for a weapon warning. After reconstruction, it is determined that the weapon is hidden at the

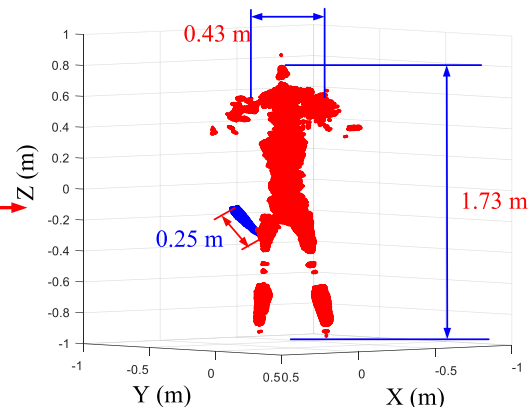## Silhouette and local component information

Reconstruction result

FIGURE 16. The 3D reconstruction result of the human body.

TABLE 2. The Numerical Comparison Between the Reconstruction Results.

Parameters	Value	Factorization method	The proposed method
Length of l_1	27.69 m	28.88	28.63 m
Attitude vector of l_1	(-0.97,0.26,0)	Unknown	(-0.97,0.26,0)
Length of l_2	58.12 m	58.12	57.89m
Attitude vector of l_2	(1.00,0,0)	Unknown	(1.00,0,0)
Length of l_3	15.88 m	16.77	16.26 m
Attitude vector of l_3	(0,0,1.00)	Unknown	(0,0,1.00)
Scale factor b_1 (l_2/l_1)	2.10	2.01	2.02
Scale factor b_2 (l_3/l_1)	0.57	0.58	0.57

TABLE 3. The Main Parameters of the SAR Images.

Parameters	Value
Size of a single image	160×383
Image resolutions	0.005 m $\times$ 0.005 m
Bandwidth	6 GHz
Center frequency of transmit signal	27 GHz

mans waist and its length is 0.25 m. This experiment vividly illustrates the potential values of the proposed algorithm in different extended applications.

V. CONCLUSION AND FUTURE WORK

In this paper, we have proposed a 3D reconstruction algorithm based on the radar image sequence and also expanded it to handle the practical limitations of synthetic aperture manifold via the feature fusion of radar and optical images. With the accommodation of radar LOS parameters, target 3D visual hull is recovered from the extracted silhouette information in the 2D observed imagery. The feasibility of the proposed algorithm is proved with the experiment in different application scenes. Compared with the existing methods, the proposed approach reconstructs the target 3D surface with size information and meanwhile determines its absolute attitude in the target Cartesian coordinate system. In order to expand it to various practical applications, three areas ought to be further investigated in the future work.

1) Still in space applications, it should be emphasized that the proposed algorithm is devoted to handle the stable attitude satellite, whereas the reconstruction for a spinning satellite is still an essential challenge. From the previous work, it might offer access for this task with the synchronized observation of a multi-static ground-based radar system when the centroid registration of multi-static images is accomplished.

2) In view of the same measurement mechanism in SAR and ISAR systems, the proposed algorithm is suitable for the SAR imagery in theory. However, some technological keypoints ought to be solved in a large scene SAR measurement: the motion deviation of the SAR platform impacts the imaging plane determination; the silhouette registration in the large scene imagery needs finer image processing; the reconstruction of a large scene itself aggravates the calculation burden of the proposed algorithm, and so on.

3) In the current stage, the feature fusion of the radar and optical images is based on the high-level feature of the target, i.e. the silhouette information. In view of image fusion, the merit brought by the inherent orthographic relationship between these two sorts of imaging planes is far from that. Thus, it is meaningful to mine the deep connection of pixel-level features among these two sorts of images according to the observation geometrical manifold, for example, using the pixel density in optical imagery to handle the angular glint phenomenon in the radar imagery.

ACKNOWLEDGMENT

REFERENCES

[1] L. Carozza and A. Bevilacqua, "Error analysis of satellite attitude determination using a vision-based approach," *ISPRS J. Photogramm. Remote Sens.*, vol. 83, pp. 19–29, Sep. 2013. doi: 10.1016/j.isprsjprs.2013.05.007.

[2] K. Suwa, T. Wakayama, and M. Iwamoto, "Three-dimensional target geometry and target motion estimation method using multistatic ISAR movies and its performance," *IEEE Trans. Geosci. Remote Sens.*, vol. 49, no. 6, pp. 2361–2373, Jun. 2011.

[3] S. Sommer, J. Rosebrock, D. Cerutti-Maori, and L. Leushacke, "Temporal analysis of ENVISAT's rotational motion," in *Proc. 7th Eur. Conf. Space Debri*, Apr. 2017, pp. 1–7.

[4] M. Ferrara, G. Arnold, and M. Stuff, "Shape and motion reconstruction from 3D-to-1D orthographically projected data via object-image relations," *IEEE Trans. Pattern Anal. Mach. Intell.*, vol. 31, no. 10, pp. 1906–1912, Oct. 2009.

[5] C. Tomasi and T. Kanade, "Shape and motion from image streams under orthography: A factorization method," *Int. J. Comput. Vis.*, vol. 9, no. 2, pp. 137–154, Nov. 1992.

[6] F. E. Mcfadden, "Three-dimensional reconstruction from ISAR sequences," in *Proc. Int. Soc. Opt. Photon.* Eldeniya, Sri Lanka: AeroSense, 2002.

[7] S. Lemmens, H. Krag, J. Rosebrock, and I. Carnelli, "Radar mappings for attitude analysis of objects in orbit," in *Proc. 6th Eur. Conf. Space Debris*, Darmstadt, Germany, Apr. 2013, pp. 20–24.

[8] F. Wang, F. Xu, and Y.-Q. Jin, "three-dimensional reconstruction from a multiview sequence of sparse ISAR imaging of a space target," *IEEE Trans. Geosci. Remote Sens.*, vol. 56, no. 2, pp. 611–620, Feb. 2018.

[9] Y. Zhou, L. Zhang, Y. Cao, and Z. Wu, "Attitude estimation and geometry reconstruction of satellite targets based on ISAR image sequence interpretation," *IEEE Trans. Aerosp. Electron. Syst.*, to be published.

[10] Y. Zhou, L. Zhang, and Y. Cao, "Attitude estimation for space targets by exploiting the quadratic phase coefficients of inverse synthetic aperture radar imagery," *IEEE Trans. Geosci. Remote Sens.*, to be published.

[11] D. Kucharski *et al.*, "Attitude and spin period of space debris envisat measured by satellite laser ranging," *IEEE Trans. Geosci. Remote Sens.*, vol. 52, no. 12, pp. 7651–7657, Dec. 2014.

[12] C. D. Austin, E. Ertin, and R. L. Moses, "Sparse signal methods for 3-D radar imaging," *IEEE J. Sel. Topics Signal Process.*, vol. 5, no. 3, pp. 408–423, Jun. 2011.

[13] D. G. Macfarlane and D. A. Robertson, "A 94 GHz real aperture 3D imaging radar," in *Proc. Eur. Radar Conf.*, Manchester, U.K., Sep. 2006, pp. 154–157.

[14] D. Bleh *et al.*, "A 100 GHz FMCW MIMO radar system for 3D image reconstruction," in *Proc. Eur. Radar Conf. (EuRAD)*, London, U.K., Oct. 2016, pp. 37–40.

[15] M. Pinheiro, P. Prats, R. Scheiber, M. Nannini, and A. Reigber, "Tomographic 3D reconstruction from airborne circular SAR," in *Proc. IEEE Int. Geosci. Remote Sens. Symp.*, Cape Town, South Africa, Jul. 2010, pp. III-21–III-24.

[16] H. C. Yin and P. K. Huang, "Further comparison between two concepts of radar target angular glint," *IEEE Trans. Aerosp. Electron. Syst.*, vol. 44, no. 1, pp. 372–380, Jan. 2008.

[17] J. T. Mayhan, M. L. Burrows, K. M. Cuomo, and J. E. Piou, "High resolution 3D 'snapshot' ISAR imaging and feature extraction," *IEEE Trans. Aerosp. Electron. Syst.*, vol. 37, no. 2, pp. 630–642, Apr. 2001.

[18] K. Grauman, G. Shakhnarovich, and T. Darrell, "A Bayesian approach to image-based visual hull reconstruction," in *Proc. Comput. Soc. Conf. Comput. Vis. Pattern Recognit.*, Jun. 2003, pp. I-187–I-194.

[19] A. Laurentini, "The visual hull concept for silhouette-based image understanding," *IEEE Trans. Pattern Anal. Mach. Intell.*, vol. 16, no. 2, pp. 150–162, Feb. 1994.

[20] S. M. Seitz, B. Curless, J. Diebel, D. Scharstein, and R. Szeliski, "A comparison and evaluation of multi-view stereo reconstruction algorithms," in *Proc. IEEE Comput. Soc. Conf. Comput. Vis. Pattern Recognit.*, Jun. 2006, pp. 519–528.

[21] S. N. Sinha and M. Pollefeys, "Multi-view reconstruction using photo-consistency and exact silhouette constraints: A maximum-flow formulation," in *Proc. 10th IEEE Int. Conf. Comput. Vis. (ICCV)*, Oct. 2005, pp. 349–356.

[22] J.-S. Franco and E. Boyer, "Fusion of multiview silhouette cues using a space occupancy grid," in *Proc. 10th IEEE Int. Conf. Comput. Vis. (ICCV)*, Oct. 2005, pp. 1747–1753.

[23] H. Aliakbarpour, V. B. S. Prasath, K. Palaniappan, G. Seetharaman, and J. Dias, "Heterogeneous multi-view information fusion: Review of 3-D reconstruction methods and a new registration with uncertainty modeling," *IEEE Access*, vol. 4, pp. 8264–8285, 2016.

[24] T.-N. Nguyen, H.-H. Huynh, and J. Meunier, "3D reconstruction with time-of-flight depth camera and multiple mirrors," *IEEE Access*, vol. 6, pp. 38106–38114, 2018.

[25] Z. Xu, L. Wu, M. Gerke, R. Wang, and H. Yang, "Skeletal camera network embedded structure-from-motion for 3D scene reconstruction from UAV images," *ISPRS J. Photogramm. Remote Sens.*, vol. 121, pp. 113–127, Nov. 2016.

[26] W. Liao, F. Van Coillie, L. Gao, L. Li, B. Zhang, and J. Chanussot, "Deep learning for fusion of APEX hyperspectral and full-waveform LiDAR remote sensing data for tree species mapping," *IEEE Access*, vol. 6, pp. 68716–68729, 2018.

[27] Y. Zhan, H. Zhang, and H. Lin, "Improving the impervious surface estimation with combined use of optical and SAR remote sensing images," *Remote Sens. Environ.*, vol. 141, pp. 155–167, Feb. 2014.

[28] I. Ashraf, S. Hur, and Y. Park, "An investigation of interpolation techniques to generate 2D intensity image from LiDAR data," *IEEE Access*, vol. 5, pp. 8250–8260, 2017.

[29] S. W. Shaw, R. J. P. Defigueiredo, and K. Krishen, "Fusion of radar and optical sensors for space robotic vision," in *Proc. IEEE Int. Conf. Robot. Automat.*, vol. 3, Apr. 1998, pp. 1842–1846.

[30] H. H. Mcnairn, C. Champagne, J. Shang, D. Holmstrom, and D. Holmstrom, "Integration of optical and synthetic aperture radar (SAR) imagery for delivering operational annual crop inventories," *ISPRS J. Photogramm. Remote Sens.*, vol. 64, no. 5, pp. 434–449, Sep. 2009.

[31] S. Huang, R. L. Crabtree, C. Potter, and P. Gross, "Estimating the quantity and quality of coarse woody debris in Yellowstone post-fire forest ecosystem from fusion of SAR and optical data," *Remote Sens. Environ.*, vol. 113, no. 9, pp. 1926–1938, Sep. 2009.

[32] S. Huang, C. Potter, R. L. Crabtree, S. Hager, and P. Gross, "Fusing optical and radar data to estimate sagebrush, herbaceous, and bare ground cover in Yellowstone," *Remote Sens. Environ.*, vol. 114, no. 2, pp. 251–264, Feb. 2010.

[33] Y. Byun, J. Choi, and Y. Han, "An area-based image fusion scheme for the integration of sar and optical satellite imagery," *IEEE J. Sel. Topics Appl. Earth Observ. Remote Sens.*, vol. 6, no. 5, pp. 2212–2220, Oct. 2013.

[34] Z. Bao, M. Xing, and T. Wang, *Radar Imaging Technology*. Beijing, China: Electronics Industry, 2005, pp. 24–40.

[35] FGAN Lab, German. (Mar. 2018). *Forscher des Fraunhofer FHR Begleit-enwiedereintritt Der Chinesischen Raumstation Tiangong-1*. [Online]. Available: https://www.fhr.fraunhofer.de/tiangong-bilder

[36] Y. Ma *et al.*, *An Invitation to 3-D Vision: From Images to Geometric Models*. Springer, 2004.

[37] P. Conte, V. A. Girelli, and E. Mandanici, "Structure from motion for aerial thermal imagery at city scale: Pre-processing, camera calibration, accuracy assessment," *ISPRS J. Photogramm. Remote Sens.*, no. 146, pp. 320–333, Dec. 2018.

[38] L. Grammatikopoulos, G. Karras, and E. Petsa, "An automatic approach for camera calibration from vanishing points," *ISPRS J. Photogramm. Remote Sens.*, vol. 62, no. 1, pp. 64–76, May 2007.

[39] A. Ghobadzadeh, S. Gazor, M. R. Taban, A. A. Tadaion, and S. M. Moshtaghioun, "Invariance and optimality of CFAR detectors in binary composite hypothesis tests," *IEEE Trans. Signal Process.*, vol. 62, no. 14, pp. 3523–3535, Jul. 2014.

[40] R. Gonzalesz and R. Woods, *Digital Image Processing*. Beijing, China: Electronics Industry, 2007, pp. 432–435.

[41] A. F. Garcia-Fernandez, O. A. Yeste-Ojeda, and J. Grajal, "Facet model of moving targets for ISAR imaging and radar back-scattering simulation," *IEEE Trans. Aerosp. Electron. Syst.*, vol. 46, no. 3, pp. 1455–1467, Jul. 2010. doi: 10.1109/TAES.2010.5545200.

[42] A. Boag, "A fast physical optics (FPO) algorithm for high frequency scattering," *IEEE Trans. Antennas Propag.*, vol. 52, no. 1, pp. 197–204, Jan. 2004.

[43] S. Auer, S. Hinz, and R. Bamler, "Ray-tracing simulation techniques for understanding high-resolution SAR images," *IEEE Trans. Geosci. Remote Sens.*, vol. 48, no. 3, pp. 1445–1456, Mar. 2010.

[44] K. S. Kulpa *et al.*, "An advanced SAR simulator of three-dimensional structures combining geometrical optics and full-wave electromagnetic methods," *IEEE Trans. Geosci. Remote Sens.*, vol. 52, no. 1, pp. 776–784, Jan. 2014.

LEI ZHANG was born in Zhejiang, China, in 1984. He received the Ph.D. degree from Xidian University, in 2012, where he was an Associate Professor with the National Laboratory of Radar Signal Processing, from 2012 to 2019. He is currently an Associate Professor with the School of Electronics and Communication Engineering, Sun Yat-sen University. His research interests include radar imaging [synthetic aperture radar (SAR)/inverse SAR] and motion compensation.

CHAO XING was born in Shanxi, China, in 1991. He received the B.S. degree in electronic engineering from Xidian University, Xi'an, China, in 2015, where he is currently pursuing the Ph.D. degree in signal processing with the National Laboratory of Radar Signal Processing. His research interests include radar signal processing.

PENGFEI XIE was born in Henan, China, in 1992. He received the B.S. degree in electronic information science and technology from the Qingdao University of Technology, Qingdao, China, in 2016. He is currently pursuing the master's degree in signal processing with the National Laboratory of Radar Signal Processing, Xidian University. His research interest includes radar imaging.

YEJIAN ZHOU was born in Zhejiang, China, in 1993. He received the B.S. degree in electronic engineering from Xidian University, Xi'an, China, in 2015, where he is currently pursuing the Ph.D. degree in signal processing with the National Laboratory of Radar Signal Processing. His research interest includes inverse synthetic aperture radar imaging and image interpretation.

YUNHE CAO was born in Anhui, China. He received the B.S., M.S., and Ph.D. degrees from Xidian University, Xi'an, China, in 2001, 2004, and 2006, respectively, where he is currently a Professor with the National Laboratory of Radar Signal Processing. His research interests include MIMO radar, digital array radar, adaptive signal processing, and target detection.

• • •